

Cite this: *J. Mater. Chem. A*, 2022, **10**, 24190

Mechanism of coupled phase/morphology transformation of 2D manganese oxides through Fe galvanic exchange reaction†

Raquel Aymerich-Armengol, ^{*a} Paolo Cignoni, ^b Petra Ebbinghaus,^a Julia Linnemann, ^b Martin Rabe, ^a Kristina Tschulik, ^b Christina Scheu ^{*a} and Joohyun Lim ^{*c}

Nanostructured manganese oxides have a rich variety of morphologies and crystal phases which can undergo transformations during synthesis and application. Although these structural features are crucial for their performance, the mechanisms behind such transitions are not well understood. Herein, we describe the mechanism of transformation from layered 2D δ - MnO_2 nanosheets to the scarcely reported γ - MnO_2 nanocone morphology. Despite the common purpose of introducing Fe dopants to enhance the conductivity of layered manganese oxides, the Fe galvanic exchange reaction was found responsible for such coupled phase/morphology transition. Electrochemical characterization confirmed a distinct electrochemical behaviour of the nanocones, emphasizing the need to unravel the mechanism of 2D MnO_2 transformation. Such mechanistic insights were gained by systematic and rigorous electron microscopy studies. The effect of the local chemical composition was determined by energy dispersive X-ray spectroscopy while electron energy loss spectroscopy unravelled the key influence of the oxidation state of Mn ions within nanosheets and nanocones. We propose and demonstrate a Mn^{2+} -mediated oxidative mechanism of coupled morphology/phase transformation subjected to the equilibrium of Fe and Mn ions during galvanic exchange reaction. These findings contribute to the understanding of the growth and morphology/phase transformations of manganese oxide nanostructures, providing insights for the rational design of nanomaterials.

Received 19th August 2022
Accepted 17th October 2022

DOI: 10.1039/d2ta06552e

rsc.li/materials-a

Introduction

Nanostructured manganese oxides (MnO_2) are promising candidates for energy storage (e.g. batteries and supercapacitors),¹ environmental (e.g. pollutant removal),² and catalysis applications (e.g. oxygen evolution reaction).³ Their properties are strongly dependent on the structure, which shows high complexity due to the variety of nanomorphologies, crystal structures (distinguishing between tunnel- and layer-like structure types), chemical compositions and stoichiometries.^{3–5}

The introduction of dopants is conducted to further improve the properties of MnO_2 .^{5,6} First described by Oh *et al.*,⁷ the galvanic exchange reaction can be performed to introduce Fe dopant in nanostructured oxides, including 2D MnO_2

nanosheets.⁸ The presence of Fe enhances the electric conductivity of the MnO_2 material, which is a requirement for electrochemical applications. According to previous reports, dopant percentages of Fe up to 5 at% optimized the specific capacitance of MnO_2 .^{9–11}

Morphology and/or phase transitions can occur not only during synthesis, but also during post-synthesis procedures such as dopant modification and application of the nanostructures.^{12,13} It has been reported that the presence of certain cations can stabilize specific crystal structures, thus causing phase transformations that are often coupled with structural changes. This is the case for the layer-to-tunnel polymorphic transitions of MnO_2 , which benefit from the presence of cations of similar size occupying the tunnel void.^{14–16} Specific examples of layer-to-tunnel transformations are those triggered by the sorption of Mn^{2+} . Two mechanisms were hypothesized to explain them: on the one hand, auto-catalytic oxidation of the adsorbed Mn^{2+} on the MnO_2 surface would account for transition to Mn^{3+} enriched oxides.¹⁷ On the other hand, comproportionation between Mn^{2+} ions and Mn^{4+} of MnO_2 would also explain Mn^{3+} presence.^{18,19}

Although understanding these transformations is of utmost importance for the design of high-performing materials, the

^aMax-Planck-Institut für Eisenforschung GmbH, Max-Planck-Straße 1, 40237, Düsseldorf, Germany. E-mail: r.aymerich@mpie.de; c.scheu@mpie.de

^bFaculty of Chemistry and Biochemistry, Chair of Analytical Chemistry II, Ruhr University Bochum, 44780 Bochum, Germany

^cDepartment of Chemistry, Institute for Molecular Science and Fusion Technology, Kangwon National University, Chuncheon, Gangwon, 24341, Republic of Korea. E-mail: jlim@kangwon.ac.kr

† Electronic supplementary information (ESI) available. See DOI: <https://doi.org/10.1039/d2ta06552e>



mechanisms behind them are not yet completely unravelled.²⁰ For instance, Tu *et al.* observed a coupled phase/morphology transition upon Mn^{2+} addition from layered birnessite to several different MnO_2 structures.¹⁷ However, their synthesis methodology required several days and the exact mechanism behind the layer-to-tunnel transformation could not be proven due to lack of local structural analyses. Among the nanostructures yielding from the layer-to-tunnel transformation, MnO_2 nanocones were obtained. The nanocones consist of a hexagonal pyramid morphology with faceted faces and a ramsdellite $\gamma\text{-MnO}_2$ ²¹ or the closely related $\varepsilon\text{-MnO}_2$ ²² crystal structure. This nanostructure has since rarely been reported either arising from self-assembly of $\alpha\text{-MnOOH}$ nanorods^{21,23} or other direct wet chemical synthesis.²² Furthermore, no electrochemical structure–property relationship study was pursued for the nanocone structure.

In this work, we achieve rapid phase transformation of layered MnO_2 to $\gamma\text{-MnO}_2$ nanocones by *in situ* generation of Mn defects and Mn^{2+} ions within 2D manganese oxide nanosheets using Fe galvanic exchange reaction. To investigate the phase transformation mechanism, extensive local structural and chemical characterization of the nanostructures was conducted by electron microscopies (scanning electron microscopy (SEM), (scanning) transmission electron microscopy ((S)TEM) and spectroscopic techniques (energy dispersive X-ray (EDS), electron energy loss spectroscopy (EELS) and Raman spectroscopy). The results allowed us to describe a Mn^{2+} -mediated oxidative mechanism for the nanosheet to nanocone morphology *via* galvanic exchange reaction. Our findings shed light into the mechanism behind coupled phase/morphology transitions of MnO_2 , which is crucial for building structure–property relationships of functional nanomaterials.

Experimental section

Materials

The materials used during synthesis were tetramethylammonium hydroxide (TMAOH, 25 wt% in water, Sigma-Aldrich), hydrogen peroxide (H_2O_2 , 30 wt%, Merck), manganese chloride ($\text{MnCl}_2 \cdot 4\text{H}_2\text{O}$, >98%, Sigma-Aldrich), hydrochloric acid (HCl, 37 wt%, VWR), iron sulphate ($\text{FeSO}_4 \cdot 7\text{H}_2\text{O}$, >98%, Sigma-Aldrich), tetramethylammonium chloride (TMACl, >98%, Sigma-Aldrich) and ethanol (EtOH, >99.8%, Carl Roth).

To prepare the working electrodes 1-methyl-2-pyrrolidone (NMP, >99%, Alfa Aesar) and Nafion® 117 solution ($\approx 5\%$ in mixture of lower aliphatic alcohols, Sigma-Aldrich) were used. The electrolyte for the electrochemical measurements was prepared from potassium sulphate (K_2SO_4 , AnalaR NORMA-PUR, VWR).

Synthesis

MnO_2 nanosheets synthesis.^{8,24} To prepare ~ 60 ml of product, a mixture of 43 ml of a solution of 0.6 M TMAOH and 3 wt% H_2O_2 was added slowly to 16 ml of a 0.3 M $\text{MnCl}_2 \cdot 4\text{H}_2\text{O}$ solution. The dark brown mixture was let to stir from 15 h (HMO, 1M-HMO) to 24 h (2M-HMO, 3M-HMO) and was

centrifuged for 8 min at 3800 rpm either immediately (1M-HMO, 2M-HMO) or after 24 h (FMO, 3M-HMO). The supernatant suspension was aggregated with HCl 36 wt% (*ca.* 0.8 ml). This solution was centrifugated for 4 min at 5000 rpm and the aggregates were redispersed in deionized water and in EtOH. Finally, the aggregates in the solution were dried for 6.5 h in an oven preheated at 110 °C and the powder was grinded in an agate mortar.

Fe galvanic exchange.⁸ Typically, 0.5 ml of a $\text{FeSO}_4 \cdot 7\text{H}_2\text{O}$ precursor solution of concentration in the range of 2–25 mg ml^{-1} were injected to 5 ml of MnO_2 nanosheets suspension (1 mg ml^{-1}). To test the effect of pH and cations, 1.7×10^{-5} mol of either TMAOH (6 μL) or TMACl (1.8 mg) were added to the MnO_2 solution prior to Fe addition. In all cases, immediately after Fe addition the solution was heated to 90 °C (heating rate 3 °C min^{-1}) while stirring for 2 h.

Aging of the materials. After Fe galvanic exchange reaction, the suspension was let to age for 24 h. The materials were subsequently purified with centrifugation and redispersion cycles in deionized water and EtOH.

Electrochemical characterization

Cyclic voltammograms (CVs) were recorded with a three electrodes setup connected to a BioLogic VSP-300 potentiostat. A homemade Ag/AgCl, 3 M KCl electrode ($E = 0.210$ V *vs.* SHE) equipped with 0.5 M K_2SO_4 double junction was used as a reference electrode and a graphite rod ($d = 8$ mm) was used as a counter electrode. The CVs were acquired using an analog scan rate of 25 mV s^{-1} between 0.0 – 0.8 V *vs.* Ag/AgCl, 3 M KCl with a 0.5 M K_2SO_4 solution as an electrolyte. The working electrodes were prepared on a glass slide substrate (0.2 mm thickness, 18 mm diameter) coated with a 200 nm layer of gold and with an 8 nm Ti adhesion layer. 10 μL of a dispersion of 10 mg ml^{-1} of the active material and a 1 mg ml^{-1} of Nafion® in NMP were drop cast in the middle of the electrode slide in four 1.5 μL and two 2.0 μL steps. The functionalized electrodes were loaded in a custom-made teflon cell leaving exposed to the electrolyte solution the central area of the working electrode ($d = 10$ mm).²⁵ A schematic of the cell is shown in Fig. S1.† The potentials were converted to the SHE scale for graph preparation.

Structural characterization

Electron microscopy. SEM micrographs were acquired in a ZEISS Gemini with an acceleration voltage of 1.5 kV using an in-lens secondary electron detector. High resolution TEM (HRTEM) and scanning transmission electron microscopy high angle annular dark field (STEM-HAADF) were conducted in two FEI Titan Themis 60–300 with a C_s corrector for the objective and condenser lenses, respectively. EDS was performed with the Bruker Super X-EDX detector of the microscopes while EELS was acquired at the probe corrected STEM with a Gatan Quantum ERS energy filter. To check any possible reduction by the electron beam on the thin nanostructures, experiments were performed on nanosheets and nanocones of various thickness. The results can be found on Fig. S2.† Since no severe reduction was



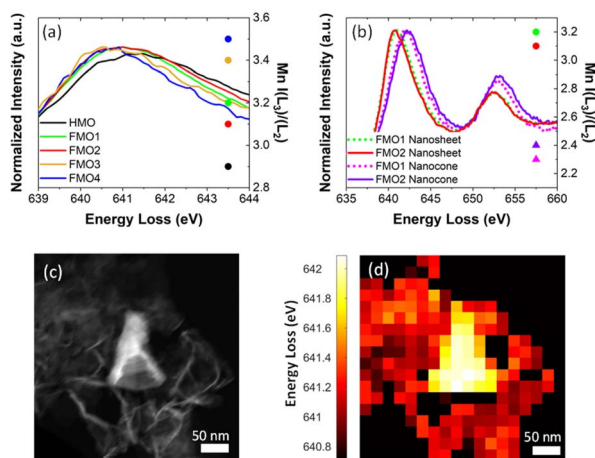


Fig. 4 (a) Left-Y axis: EELS Mn L_3 white line of the nanosheets of each material. Right-Y axis: intensity ratio of Mn L_3 and L_2 peaks (b) Left-Y axis: EELS Mn $L_{2,3}$ white lines of nanosheets and nanocones of FMO1 and FMO2. Right-Y axis: intensity ratio of Mn L_3 and L_2 peaks for FMO1 and FMO2 nanocones and nanosheets. (c and d) HAADF and corresponding EELS mapping after PCA analysis showing the local energy loss corresponding to Mn L_3 of the nanosheets and nanocones.

FMO1, FMO2, FMO3 and FMO4. The spectra show a shift of Mn L_3 between the materials with Fe (Table 1) and HMO, indicating that upon galvanic exchange there are enhanced contributions of lower Mn valences ($\text{Mn}^{3+}/\text{Mn}^{2+}$) due to the partial substitution of Mn^{4+} by Fe^{3+} . These qualitative results were also confirmed by $I(L_3)/I(L_2)$ ratios, the reference values of which decrease from $I(L_3)/I(L_2)_{\text{MnO}} \approx 4.0$, $I(L_3)/I(L_2)_{\text{Mn}_2\text{O}_3} \approx 2.5$ to $I(L_3)/I(L_2)_{\text{MnO}_2} \approx 1.9$.³⁰ The calculated ratios shown in Fig. 4a and Table 1 increase from 2.9 to 3.5 with Fe, thus showing more reduction following the higher Fe content.

The value of $I(L_3)/I(L_2)_{\text{HMO}} \approx 2.9$ indicates that the Mn ions in HMO before addition of Fe are already in a very low valence, with significant $\text{Mn}^{2+}/\text{Mn}^{3+}$ contributions. This is compatible with a birnessite structure containing hydrated cations in the interlayer to compensate $\text{Mn}^{3+}/\text{Mn}^{4+}$ or $\text{Mn}^{2+}/\text{Mn}^{4+}$ of the structure, characteristic of the synthesis methodology.^{33,34}

EELS spectra show a Mn L_3 peak shift as high as ~ 1.1 eV for FMO1 and ~ 1.3 eV for FMO2 between nanocones and nanosheets (Fig. 4b, Table 1). This difference is also seen by local PCA of an EELS mapping of a nanocone and nanosheets²⁹ (Fig. 4c and d) with data displaying the energy loss of the Mn L_3 peak maximum as indicator of oxidation state. Such results clearly reveal that Mn ions in the nanocones are more oxidized than those in assembled nanosheets. This is confirmed by the distinct changes of intensity ratios from $I(L_3)/I(L_2)_{\text{FMO1}} \approx 3.2$ and $I(L_3)/I(L_2)_{\text{FMO2}} \approx 3.1$ for nanosheets to $I(L_3)/I(L_2)_{\text{FMO1}} \approx 2.3$ and $I(L_3)/I(L_2)_{\text{FMO2}} \approx 2.4$ for nanocones. The magnitude of the difference between Mn oxidation state in assembled nanosheets and nanocones can neither be explained solely by the different Fe content nor by a difference in their thicknesses (Fig. S2[†]). Therefore, these results strongly indicate the oxidation of the Mn ions during morphology transformation from 2D MnO_2 nanosheet to nanocones.

Crystal structure

To elucidate the crystal structure of the materials, confocal Raman spectroscopy measurements were conducted (Fig. 5). All the spectra show four active modes: ν_1 ($721.6\text{--}744.9\text{ cm}^{-1}$), ν_2 ($636.2\text{--}643.0\text{ cm}^{-1}$), ν_3 ($566.9\text{--}573.0\text{ cm}^{-1}$), and ν_4 ($487.1\text{--}500.8\text{ cm}^{-1}$) (Table S1[†]). These modes can be assigned to the layered birnessite $\delta\text{-MnO}_2$ structure for all FMO1, FMO2, FMO3 and FMO4 despite the different Fe contents.^{8,34,35} X-ray diffraction (XRD) also confirmed such phase in HMO (Fig. S11[†]).

Moreover, Raman ν_1 and ν_2 modes appear broader in the materials with higher Fe contents (FMO3 and FMO4). This result is compatible with a higher extend of galvanic exchange reaction with higher Fe ratios, which induces the formation of more Mn defects and Mn^{2+} cations. Such defects reduce the order of the lattice, resulting in a polycrystalline structure with smaller grain sizes which broaden the Raman peaks.³⁴ The smaller grain size of the materials with higher Fe content was also confirmed by TEM imaging the materials (Fig. S12[†]).

Local crystal structure investigations of the nanocones and the nanosheets were conducted by HRTEM, Fast Fourier Transform (FFT) (Fig. 6a–f and S13[†]) and selected area aperture electron diffraction (SAED) (Fig. 6g and h). The data indicates that the assembled nanosheets of HMO as well as nanosheets containing Fe (FMO1, FMO2, FMO3 and FMO4) show a polycrystalline birnessite structure (Fig. S14[†]) while nanocones are highly crystalline *e.g.* much larger crystal size. The nanocone



Fig. 5 Raman spectra of HMO, FMO1, FMO2, FMO3 and FMO4.





Fig. 6 (a and b) HRTEM micrograph and corresponding FFT pattern of a HMO nanosheet. (c–f) HRTEM micrographs and FFT patterns corresponding to two facets of a FMO2 nanocone. (g and h) TEM micrograph and corresponding SAED pattern of a FMO2 nanocone.

patterns could be assigned to the γ - MnO_2 ramsdellite crystal structure (orthogonal phase with $a = 4.51$, $b = 9.26$, $c = 2.86$, space group Pbnm (62)), in agreement with previous reports.²¹ The nanocone planes were determined to be the (1–10) for the facets of the nanocone with a twinning along the $\langle 021 \rangle$ direction and the (100) facet on the base. This confirms that a coupled morphology and phase transition occurs upon Fe galvanic exchange reaction.

Nanocone growth mechanism from galvanic exchange reaction

With the results of the morphological and chemical analyses of $\text{Fe}_x\text{Mn}_{1-x}\text{O}_2$ nanosheets and nanocones, we hypothesize the following mechanism for the coupled morphology/phase transformation (Fig. 7). During the galvanic exchange reaction, Fe^{2+} reduces Mn^{4+} , yielding Fe^{3+} and Mn^{2+} . The fate and equilibrium of these cations is key for obtaining one morphology or the other. As demonstrated by the EDS analyses, when the initial Fe^{2+} to MnO_2 nanosheets ratio is high, the only outcome are nanosheets with large Fe contents (FMO3 and FMO4). This means the Fe^{3+} occupies most of the available positions in the lattice, interlayer, and adsorption sites on the surface of MnO_2 nanosheets while Mn^{2+} is dissolved in aqueous solution, yielding $\text{Fe}_x\text{Mn}_{1-x}\text{O}_2$ nanosheets as the only product. The partial dissolution of Mn^{4+} to Mn^{2+} as a consequence of Fe galvanic exchange reaction was demonstrated by performing ICP-MS on the solutions after reaction of MnO_2 with Fe. The results showed larger amounts of Mn ions in the materials with larger amounts of Fe precursor (Table S2†).

The morphological and EDS analyses revealed the phase transformation at lower Fe^{2+} to MnO_2 nanosheets ratio. At such conditions, a competition between Fe^{3+} and Mn^{2+} for the lattice and interlayer sites can occur and Mn^{2+} will also partially

occupy those sites instead of completely dissolving in solution. Upon aging for 24 h of the materials, these Mn^{2+} cations will be re-oxidized by atmospheric and water-dissolved oxygen, yielding γ - MnO_2 nanocones with low Fe contents and higher Mn oxidation states, as demonstrated by EDS and EELS analyses. Since the oxidation state of the starting layered MnO_2 nanosheet is lower than that of the nanocone product, a comproportionation mechanism for this transformation can be discarded.

To confirm the key role of the *in situ* Mn^{2+} formation we tried to reproduce the results of FMO2 by substituting Fe^{2+} for an equivalent molar percentage of Mn^{2+} (MMO2, Fig. S15†). A morphology transformation was successfully produced by Mn^{2+} , confirming it is triggered by such cation. Although the EELS and Raman analysis showed similar results in MMO2 as compared to FMO2 (Fig. S16†), instead of obtaining a defined nanocone shape the MMO2 nanostructures showed a small faceted cone-like nanoparticle morphology. This contrast with the previous results reported by Tu *et al.*,¹⁷ who could obtain nanosheet to nanocone transformation through Mn^{2+} adsorption, can be explained by their much longer aging times. Such finding highlights the role of Fe^{2+} in speeding up the transformation by generating *in situ* the Mn^{2+} species with crystal defects, thus reducing the time of synthesis of well-defined nanocones.

Finally, since the nanocone transformation occurs through an oxidative step, the original oxidation state of the 2D MnO_2 (HMO) can be of utmost importance. To assess its effect, three 2D MnO_2 materials named 1M-HMO, 2M-HMO and 3M-HMO were synthesized by modifying the synthesis and aging time (see Experimental section) in order to change their Mn oxidation state. This was monitored by EELS (Fig. 8a), demonstrating





Fig. 7 Schematic mechanism governing the synthesis of $\text{Fe}_x\text{Mn}_{1-x}\text{O}_2$ nanosheets and nanocones through galvanic exchange reaction.

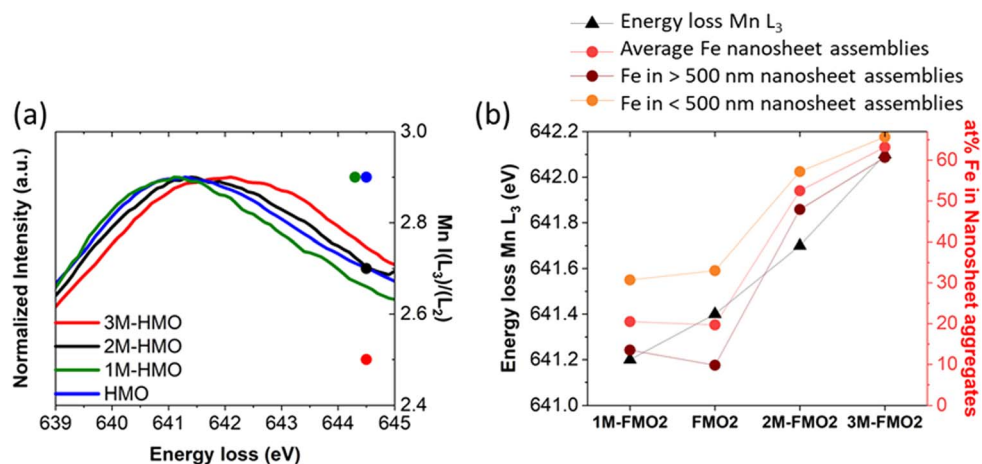


Fig. 8 (a) Left-Y Axis: EELS Mn L_3 peaks of HMO, 1M-HMO, 2M-HMO and 3M-HMO. Right-Y axis: corresponding Mn L_3/L_2 values. (b) Trends of oxidation state of xM-HMO (Left-Y axis) and Fe introduced by galvanic exchange reaction (right-Y axis) for xM-FMO2.

that the longer the synthesis and aging times, the more oxidized the Mn species of the 2D MnO_2 nanosheets.

Galvanic exchange reaction was subsequently conducted with these xM-HMO materials emulating FMO2 conditions (xM-FMO2). The results showed that the materials produced with more oxidized MnO_2 nanosheets (2M-FMO2 and 3M-FMO2) contained $\text{Fe}_x\text{Mn}_{1-x}\text{O}_2$ nanosheets with larger contents of Fe than FMO2 but containing similar ratio of nanocones (Fig. 8b and S17 \dagger). On the contrary, reducing the oxidation state of Mn species (1M-HMO) by shorter synthesis and aging time resulted on materials with the same 20 at% Fe than HMO after galvanic exchange reaction. However, the difference in oxidation state of 1M-HMO contributed to the major enhancement of the

nanocone morphology with respect to nanosheet after reaction (Fig. S17 \dagger). These results can be related to the galvanic exchange reaction potentials with different Mn^{m+} species. The reaction between $\text{Fe}^{3+}/\text{Fe}^{2+}$ and $\text{Mn}_2\text{O}_3/\text{Mn}^{2+}$ couples is thermodynamically more favourable than that of $\text{Fe}^{3+}/\text{Fe}^{2+}$ and $\text{MnO}_2/\text{Mn}^{2+}$ ($\Delta E^0_{\text{cell}} = 0.714$ V vs. $\Delta E^0_{\text{cell}} = 0.459$ V, respectively). This difference potentially indicates larger local concentration of produced Mn^{2+} during galvanic exchange reaction with the more reduced 1M-HMO due to the higher thermodynamic driving force, explaining the larger nanocone to nanosheet ratio. Moreover, the nanocone size is also larger, showing an average length 391 ± 197 nm and average width 228 ± 91 nm distributed in two different family sizes. (Fig. S4 \dagger).



Conclusions

A rapid layer-to-tunnel transformation from δ -MnO₂ nano-sheets to γ -MnO₂ nanocones was achieved *via* Fe galvanic exchange reaction. Such transformation leads to a change of the electrochemical capacitive properties of the Fe_xMn_{1-x}O₂ nano-materials. Mechanistic insights were gained by a combination of electron microscopy and spectroscopy techniques. According to local EELS analyses, the coupled morphology and phase transition followed an *in situ* Mn²⁺ generation and reoxidation mechanism. Investigations on the oxidation state of the MnO₂ nanosheets and the ratio between Fe²⁺ and MnO₂ for galvanic exchange reaction revealed the major role of the equilibrium between the generated Mn²⁺ and Fe³⁺ cations for the layer-to-tunnel transition, allowing to tune the nanostructures obtained. This work highlights the importance of mechanistic understanding for the rational design, synthesis, and structure-property relationships of functional nanomaterials.

Author contributions

R. A. A. conducted the synthesis, electron microscopy experiments and data analysis and was assisted by J. L. (J. Lim) and C. S. for the results interpretation. P. C. and R. A. A. performed the electrochemical measurements. K. T. and J. L. (J. Linnenmann) assisted in the interpretation of the electrochemistry data. P. E. conducted the Raman spectroscopy experiments which were analyzed and interpreted by R. A. A. and M. R. R. A. A. wrote the manuscript with contributions of all authors. All authors have given approval to the final version of the manuscript.

Conflicts of interest

There are no conflicts to declare.

Acknowledgements

Benjamin Breitbach is acknowledged for XRD measurements. We also thank Andrea Mingers for performing ICP-MS. R. A. A. and P. C. are grateful for financial support from the International Max Planck Research School for Interface Controlled Materials for Energy Conversion (IMPRS-SurMat). R. A. A. work was supported by a fellowship of the German Academic Exchange (DAAD). K. Tschulik acknowledges funding through a Max Planck Fellowship and J. Linnenmann through the Stiftung Mercator (18023). M. Rabe work was funded by the Deutsche Forschungsgemeinschaft (DFG, German Research Foundation) under Germany's Excellence Strategy - EXC 2033 - 390677874 - RESOLV. This work was supported by the National Research Foundation of Korea (NRF) grant funded by the Korea government (MSIT) (No. NRF-2021R1F1A1061943).

References

- 1 C. M. Julien and A. Mauger, *Nanomaterials*, 2017, **7**, 396.
- 2 R. Yang, Y. Fan, R. Ye, Y. Tang, X. Cao, Z. Yin and Z. Zeng, *Adv. Mater.*, 2021, **33**, 2004862.

- 3 Y. Meng, W. Song, H. Huang, Z. Ren, S.-Y. Chen and S. L. Suib, *J. Am. Chem. Soc.*, 2014, **136**, 11452–11464.
- 4 P. K. Gupta, A. Bhandari, S. Saha, J. Bhattacharya and R. G. S. Pala, *J. Phys. Chem. C*, 2019, **123**, 22345–22357.
- 5 Z. Ye, T. Li, G. Ma, Y. Dong and X. Zhou, *Adv. Funct. Mater.*, 2017, **27**, 1704083.
- 6 L. Tian, X. Zhai, X. Wang, J. Li and Z. Li, *J. Mater. Chem. A*, 2020, **8**, 14400–14414.
- 7 M. H. Oh, T. Yu, S.-H. Yu, B. Lim, K.-T. Ko, M.-G. Willinger, D.-H. Seo, B. H. Kim, M. G. Cho, J.-H. Park, K. Kang, Y.-E. Sung, N. Pinna and T. Hyeon, *Science*, 2013, **340**, 964–968.
- 8 J. Lim, J. M. Lee, B. Park, X. Jin and S.-J. Hwang, *Nanoscale*, 2017, **9**, 792–801.
- 9 H. Liu, W. Gu, B. Luo, P. Fan, L. Liao, E. Tian, Y. Niu, J. Fu, Z. Wang, Y. Wu, G. Lv and L. Mei, *Electrochim. Acta*, 2018, **291**, 31–40.
- 10 D. P. Dubal, W. B. Kim and C. D. Lokhande, *J. Phys. Chem. Solids*, 2012, **73**, 18–24.
- 11 Y. Wang, Y.-Z. Zhang, Y.-Q. Gao, G. Sheng and J. E. ten Elshof, *Nano Energy*, 2020, **68**, 104306.
- 12 S. Birgisson, D. Saha and B. B. Iversen, *Cryst. Growth Des.*, 2018, **18**, 827–838.
- 13 T. Hatakeyama, H. Li, N. L. Okamoto, K. Shimokawa, T. Kawaguchi, H. Tanimura, S. Imashuku, M. Fichtner and T. Ichitsubo, *Chem. Mater.*, 2021, **33**, 6983–6996.
- 14 D. A. Kitchaev, S. T. Dacek, W. Sun and G. Ceder, *J. Am. Chem. Soc.*, 2017, **139**, 2672–2681.
- 15 Y.-F. Li, S.-C. Zhu and Z.-P. Liu, *J. Am. Chem. Soc.*, 2016, **138**, 5371–5379.
- 16 B. He, G. Cheng, S. Zhao, X. Zeng, Y. Li, R. Yang, M. Sun and L. Yu, *J. Solid State Chem.*, 2019, **269**, 305–311.
- 17 S. Tu, G. J. Racz and T. B. Goh, *Clays Clay Miner.*, 1994, **42**, 321–330.
- 18 P. Yang, S. Lee, J. E. Post, H. Xu, Q. Wang, W. Xu and M. Zhu, *Geochim. Cosmochim. Acta*, 2018, **240**, 173–190.
- 19 E. J. Elzinga, *Environ. Sci. Technol.*, 2011, **45**, 6366–6372.
- 20 Y. Yuan, K. He, B. W. Byles, C. Liu, K. Amine, J. Lu, E. Pomerantseva and R. Shahbazian-Yassar, *Chem*, 2019, **5**, 1793–1805.
- 21 D. Portehault, S. Cassaignon, E. Baudrin and J.-P. Jolivet, *Cryst. Growth Des.*, 2009, **9**, 2562–2565.
- 22 Y.-S. Ding, X.-F. Shen, S. Gomez, H. Luo, M. Aindow and S. L. Suib, *Adv. Funct. Mater.*, 2006, **16**, 549–555.
- 23 D. Portehault, S. Cassaignon, E. Baudrin and J.-P. Jolivet, *J. Mater. Chem.*, 2009, **19**, 7947–7954.
- 24 K. Kai, Y. Yoshida, H. Kageyama, G. Saito, T. Ishigaki, Y. Furukawa and J. Kawamata, *J. Am. Chem. Soc.*, 2008, **130**, 15938–15943.
- 25 F. Karnbach, M. Uhlemann, A. Gebert, J. Eckert and K. Tschulik, *Electrochim. Acta*, 2014, **123**, 477–484.
- 26 P. A. van Aken and B. Liebscher, *Phys. Chem. Miner.*, 2002, **29**, 188–200.
- 27 S. Devaraj and N. Munichandraiah, *J. Phys. Chem. C*, 2008, **112**, 4406–4417.
- 28 T. Brousse, M. Toupin, R. Dugas, L. Athouël, O. Crosnier and D. Bélanger, *J. Electrochem. Soc.*, 2006, **153**, A2171.



- 29 S. Zhang and C. Scheu, *Microsc*, 2017, **67**, i133–i141.
- 30 H. Tan, J. Verbeeck, A. Abakumov and G. Van Tendeloo, *Ultramicroscopy*, 2012, **116**, 24–33.
- 31 J. Lim, X. Jin, S.-J. Hwang and C. Scheu, *Adv. Funct. Mater.*, 2020, **30**, 2003849.
- 32 C. Wang, Y. Wang, X. Liu, H. Yang, J. Sun, L. Yuan, G. Zhou and F. Rosei, *Nanotechnology*, 2015, **27**, 035702.
- 33 S. Min and Y. Kim, *Minerals*, 2020, **10**, 884.
- 34 C. Julien, M. Massot, R. Baddour-Hadjean, S. Franger, S. Bach and J. P. Pereira-Ramos, *Solid State Ionics*, 2003, **159**, 345–356.
- 35 C. M. Julien, M. Massot and C. Poinignon, *Spectrochim. Acta, Part A*, 2004, **60**, 689–700.

